Multidimensional modeling of transverse avalanche laser discharges: Applications to the HgBr laser

M. J. Kushner, A. L. Pindroh, C. H. Fisher, T. A. Znotins, and J. J. Ewing
Spectra Technology, Inc. (formerly Mathematical Sciences Northwest, Inc.), 2755 Northup Way, Bellevue, Washington 98004

(Received 1 October 1984; accepted for publication 1 November 1984)

Geometrical considerations are important with respect to the stability and efficiency of avalanche electric discharge lasers. Parameters such as the electrode contours and the distribution of preionization electrons affect excitation rates through the relative values of the local electric field, local depletion of initial species, and through the response of the discharge circuitry to spatially dependent conditions within the plasma. Constriction of the discharge and subsequent impedance mismatch of the discharge to the pulse forming line result from these spatial nonuniformities. In this paper geometrical effects in the mercury bromide electric discharge laser are examined by comparing the results from a multidimensional discharge and kinetics model with experimental observations. The code models electron and heavy particle kinetics and laser intensity in time and one spatial dimension: parallel to the electrodes and perpendicular to the optical axis. Quantities whose spatial dependence is perpendicular to this dimension, such as the contours of the electrodes, are accounted for through their impact on the local electric field. HgBr laser efficiency and spatial characteristics are examined as a function of stored electrical energy, the impedance of the pulse-forming circuitry, electrode contours, and profile of the preionization electron density. Parasitic discharges within the gas, but exterior to the optical cavity, are examined as a mechanism through which the magnitude of the preionization density can effect laser efficiency.

I. INTRODUCTION

The HgBr avalanche discharge laser, which emits at 502 nm, was first demonstrated by Schimitschek and Celto.[1] Early development of the laser focused on use of UV preionized discharges,[1–3] *e*-beam sustained discharges,[4–6] direct *e*-beam pumping,[7] and UV photolytic dissociation of $HgBr_2$[8] as excitation mechanisms for the upper laser level, $HgBr(B^2\Sigma^+_{1/2})$. UV preionized HgBr lasers were able to obtain an efficiency of 1%.[3] Significantly larger laser pulse energies and efficiencies (10 J at 2%) were obtained with *e*-beam sustained discharges.[6] Further development of the avalanche discharge laser required a new preionization scheme capable of uniformly preparing large volumes of gas while being compatible with long continuous operation. X-ray preionization satisfied these needs and resulted in scaling the electric discharge laser at our laboratory to 2.5 J with an efficiency of 2.0%, and a maximum pulse energy of 3.2 J with an efficiency of 1.4%.[9,10]

During development of the HgBr laser, many geometrically dependent phenomena were observed.[6,11] The spatial extent and magnitude of fluorescence and laser intensity were observed to be functions of the shape of the electrodes, gas mix, preionization electron density, and rate of energy deposition. Constriction of the discharge, impedance matching of the discharge to the pulse-forming line, and parasitic corona discharges were also observed to be functions of these parameters. Previously reported models of the HgBr laser[6,12–15] address some of these issues for avalanche[12] and *e*-beam sustained[15] lasers. Geometrical effects in avalanche discharge lasers, though, are not addressed. The necessity to understand these geometrical effects and so maximize the efficiency of the HgBr avalanche discharge laser motivated the development of the model which we describe in this paper. In this model, the impact of electrode shapes, preionization electron density distribution, and other geometrical factors can be evaluated. To achieve this, the spatial dependence of electron and heavy particle kinetics and laser intensity are modeled in time and in the dimension parallel to the electrode surfaces and perpendicular to the optical axis. Geometrical factors whose dependence is in the direction perpendicular to this dimension, such as electrode contours, are self-consistently accounted for by calculating their effect on the applied electric field. The spatial dependence of these variables directly impact the coupling of energy from the pulse-forming line into the discharge. A spatially dependent impedance model for the discharge as a circuit element was also developed to include this effect.

The model is conceptually a compendium of four submodels. The first is a model for the electric discharge circuit. In this model, the laser head appears as a network of circuit elements and the plasma appears as a time varying resistance at the termination of a pulse-forming network (PFN). The second is a model for heavy particle and electron collision kinetics in the plasma region and includes a solution of Boltzmann's equation for the electron distribution function. Geometrical effects within the discharge (i.e., electrode separation and contours) are incorporated into this portion of the model. The connection between this portion of the model and that for the discharge circuit is through the value of resistance for the interelectrode region, computed from the electron density and the electron collision frequency obtained from the kinetics subroutines. These portions are also connected through the value of applied electric field between the electrodes, a value obtained from the circuit subroutines and required for solution of Boltzmann's equation. The third submodel is for the laser photon flux. This submodel is coupled to the kinetics through saturation of the laser transition. Finally, the fourth submodel is an analysis of parasitic dis-

 0021-8979/85/072406-18$02.40

charges which occur during the current pulse. These parasitics are streamers or corona in the gas but outside the optical cavity, and in part explain the dependence of laser pulse energy on the preionization electron density. This submodel appears in the circuit model as a resistance parallel to that of the laser discharge plasma. It is coupled to the kinetics within the laser cavity through the change in applied electric field manifested by the additional parallel resistance it represents.

The model is described in detail in Sec. II. Results from the model are discussed in the following three sections. In Sec. III, results from the model are compared to experimental data obtained on our 1-m-long electric discharge laser. The influence of power loading, electrode shapes, preionization density profile, discharge constriction, and impedance matching of the discharge to the pulse forming line are discussed in Sec. IV. In Sec. V, the effects of parasitic discharge formation on the performance of the laser are discussed. Concluding remarks are in Sec. VI.

II. DESCRIPTION OF THE MODEL AND EXCITATION MECHANISMS

In the experimental device, electrical energy is stored in a solid dielectric pulse-forming line (PFL). The energy is switched into the laser head by triggering a pair of 40-cm-long rail gaps. The laser head has a transition section which geometrically matches the rail-gap switches to the 1-m-long discharge region. Therefore, it has associated with it geometrical inductance and capacitance as well as series and parallel resistances. At the termination of the PFL is the laser discharge region, a set of parallel electrodes separated by about 6 cm. The width of the discharge region, 4–6 cm, is determined by the spatial extent of preionizing x rays.

A. Electric discharge circuit

The PFL used in the experimental device was modeled as a pulse-forming network (PFN) with N stages (see Fig. 1). Each stage of the PFN had identical capacitance and inductance values chosen according to

$$C_{\mathrm{PFN}} = \tau/(2NZ), \tag{1}$$

$$L_{\mathrm{PFN}} = Z\tau/2N, \tag{2}$$

where Z and τ are the impedance and electrical length of the laboratory PFL. For typical operating conditions ($Z = 0.96\ \Omega$, $\tau = 145$ ns, $N = 10$), $C_{\mathrm{PFN}} = 7.5$ nF, and $L_{\mathrm{PFN}} = 7.0$ nH.

The rail-gap switch was modeled as a constant inductance and a time dependent series resistance. The resistance of the rail gap was given by

$$R_g = R_{go} + R_{gs}\exp(-t/T_s), \tag{3}$$

where t is measured from the time at which the rail gap is triggered. The values for R_{go}, R_{gs}, and T_s were obtained in the following manner. The discharge electrodes were shorted and the rail-gap triggered. Voltage and current waveforms were recorded. The circuit model was then parameterized, adjusting R_{go}, R_{gs}, and T_s until satisfactory agreement was obtained. Typical values for these quantities are $R_{gs} = 100\ \Omega$, $R_{go} = 0.01\ \Omega$, and $T_s = 5$ ns.

The major components in the circuit model of the laser head are C_H, the geometrical (or added) head capacitance; L_H, the geometrical head inductance; and R_d, the laser discharge resistance, calculated in the manner described below. Additional resistances were included in the circuit to model losses identified in the laser head. These resistances include R_1, in series with the head capacitance; R_2, parallel to the head capacitance; R_3 in series with the laser discharge; and R_4, parallel to the laser discharge. R_1 and R_2 are for the ohmic losses associated with the transition section between the solid dielectric PFL and the laser head, and R_3 accounts for the ohmic losses in the current return path from the discharge electrodes.

The parallel resistance R_4 is extremely important because the voltage drop across the discharge and, hence, the laser excitation rate is determined in large part by its value. Under idealized operating conditions, the value of R_4 is the resistance of voltage monitoring probes attached to the discharge electrodes. In this case, R_4 is constant with a large value ($> 1000\ \Omega$), and therefore would have little influence

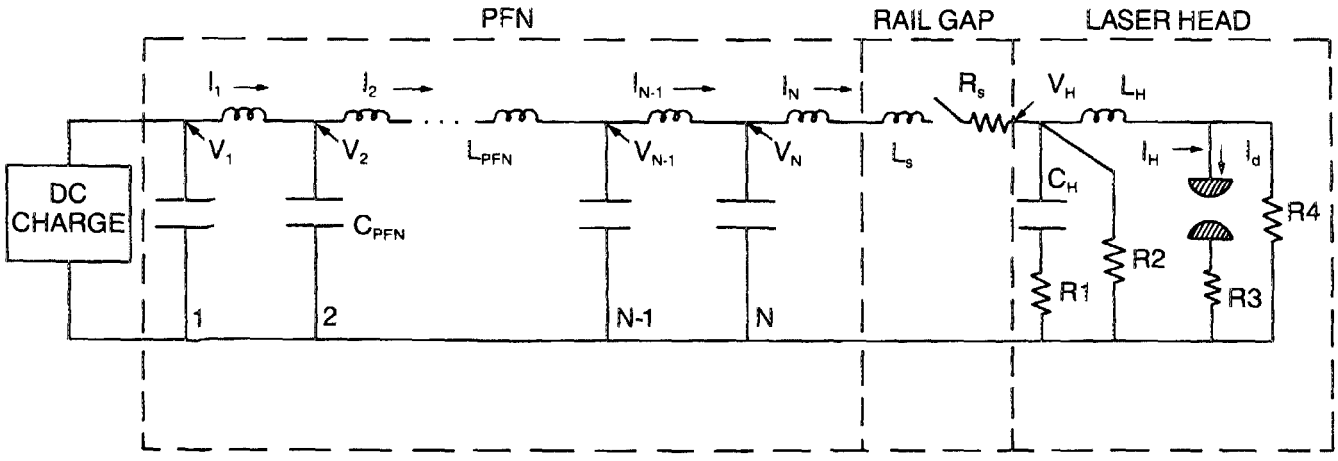

FIG. 1. Schematic of model laser discharge circuit. The continuous experimental pulse-forming line (PFL) is modeled as a ten-state pulse-forming network (PFN). dc charging of the PFN is not included in the model.

on the laser kinetics. For our experimental device, however, it was observed that a corona discharge sometimes emanated from the rear of the electrode structure, thereby providing a parallel discharge path that competed with the laser discharge between the electrodes. This parasitic discharge develops rapidly due to electric field enhancement around sharp edges on the rear of the electrode structure. When the effect of parasitic corona losses was examined, the resistance R_4 was modeled as a parallel discharge, using the same kinetics scheme as for the laser discharge. Details of this calculation will be discussed in Sec. V.

The equations solved in the model for the discharge circuitry are

$$\frac{dV_1}{dt} = \frac{-I_1}{C_{\rm PFN}}, \quad \frac{dI_1}{dt} = \frac{V_1 - V_2}{L_{\rm PFN}}, \quad i = 1, \tag{4}$$

$$\frac{dV_i}{dt} = \frac{-(I_i - I_{i-1})}{C_{\rm PFN}}, \quad \frac{dI_i}{dt} = \frac{V_i - V_{i+1}}{L_{\rm PFN}}, \quad 2 \leqslant i \leqslant N-1, \tag{5}$$

$$\frac{dV_N}{dt} = \frac{-(I_N - I_{N-1})}{C_{\rm PFN}}, \quad \frac{dI_N}{dt} = \frac{V_N - (I_N R_g + V_H)}{L_{\rm PFN} + L_s}, \quad i = N, \tag{6}$$

$$\frac{dV'_H}{dt} = \frac{I_N - \left(I_H + \dfrac{V_H}{R_2}\right)}{C_H}, \quad V_H = \frac{V'_H + (I_N - I_H)R_1}{(1 + R_1/R_2)}, \tag{7}$$

$$\frac{dI_H}{dt} = \{V_H - I_H[R_4(R_d + R_3)/(R_4 + R_d + R_3)]\}/L_H, \tag{8}$$

$$V_D = I_d R_d = \frac{I_H R_4}{(R_3 + R_4 + R_d)} \frac{R_d}{(R_3 + R_d)}. \tag{9}$$

The numeric subscripts for V and I refer to the stage number (see Fig. 1). Initial conditions for the circuit are $I_i = I_H = V_H = 0$, and $V_i = V_0$ where V_0 is the PFN charging voltage. Typical component values for the PFN and switch are $V_0 = 60$ kV, $C_{\rm PFN} = 7.5$ nF, $L_{\rm PFN} = 7.0$ nH, and $L_s = 10$ nH. R_g is given by Eq. (3). Typical component values for the laser head are $L_H = 10$ nH, $C_H = 2$ nF, $R_1 = 0.01\ \Omega$, $R_2 = 1000\ \Omega$, $R_3 = 0.01\ \Omega$, and, in the absence of a parasitic discharge, $R_4 = 1000\ \Omega$. With these values, R_3 and R_4 are only important early during the avalanche of the discharge. At this time, the electron density is low ($n_e < 10^{11}$ cm^{-3}) and the impedance of the discharge is comparable to or larger than 1000 Ω. R_3 is only important late during the high current phase of the discharge pulse when constriction and impedance collapse may occur. At this time the resistance of the discharge is reduced to as small as a tenth of an ohm.

B. Geometrical model of the laser discharge region

The laser discharge electrodes were modeled as being identical, but symmetrically opposed, conductors whose facing surfaces can be described as a center flat segment continued to the edge by a circular arc (see Fig. 2). Given these constraints, the electric field at the mid (observation) plane of the discharge is approximately given by $E = V_d/l$, where V_d is the instantaneous voltage drop across the electrodes and l is the length of the circular arc that is perpendicular to both the observation plane and the electrode surfaces. For points on the observation plane which lie between the flat segments of the electrodes, $E = V_d/d$, where d is the center electrode gap spacing. For positions on the observation plane which lie between the curved segments of the electrodes, l is given by the following:

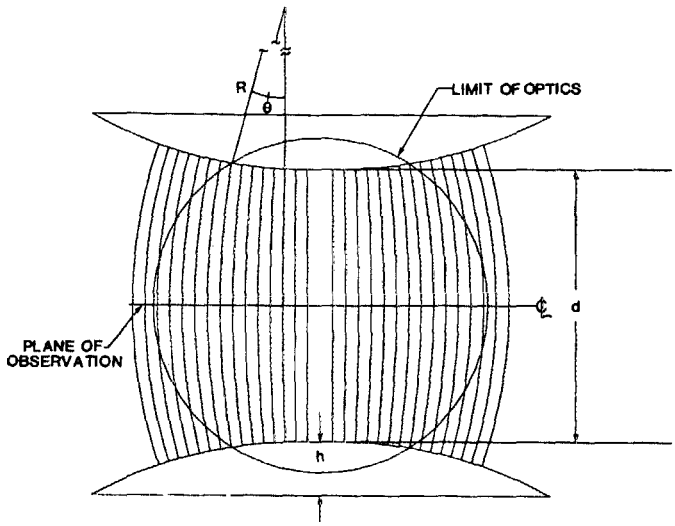

FIG. 2. Typical geometry for electrode contours. Each of the vertical lines is the boundary of a subregion in the model. R is the radius of the curved portion of the electrode. The plane of observation indicated corresponds to the spatial axis of subsequent plots in other figures.

$$l = 2b \sin\theta, \tag{10}$$

$$b = [(d/2)(d/2 + 2R) + y^2]/(2y), \tag{11}$$

$$\sin\theta = [Ry + b(d/2)]/(R^2 + b^2), \tag{12}$$

where R is the radius of curvature of the electrodes and y is the distance along the plane of observation beyond the end of the flat portion of the electrodes.

The discharge region was divided into regions whose boundaries on the observation plane are denoted by x_i. The cross-sectional area (perpendicular to the electrodes) for a region i lying between the flat portion of the electrodes is simply $A_i = (x_i - x_{i-1})d$. For a region i whose boundary lies between the curved portions of the electrodes, the cross-sectional area is given by

$$A_i = \{b_i^2[\theta_i - \sin(2\theta_i)/2] + C_i\} - \{b_{i-1}^2[\theta_{i-1} - \sin(2\theta_{i-1})/2] + C_{i-1}\}, \tag{13}$$

where b and θ are as defined above and C_i is a correction for overlap of the electrodes.

$$C_i = R^2(\theta_i - \sin(2\theta_i)/2) + R\sin\theta_i[b\sin\theta'_i - (d/2) - R(1 - \cos\theta_i)], \tag{14}$$

$$\theta'_i = \cos^{-1}[(b_i - y_i)/b_i]. \tag{15}$$

With the cross-sectional area of each region as given above, the average width of the region is defined as $w_i = A_i/l_i$.

For purposes of calculating the resistance of the discharge volume, each region was considered a separate parallel resistor. The resistance R_{di} of a particular region is

$$R_{di} = \frac{l_i m \nu_i}{w_i e^2 n_{ei} L}, \tag{16}$$

where m is the electron mass, L is the longitudinal length of the electrodes, ν_i is the electron collision frequency in region i, and n_{ei} is the electron density in region i. The last two quantities are values which are obtained from solution of the kinetic equations. The discharge resistance is then

$$R_d = 1/\sum_i (1/R_{di}) \tag{17}$$

and the voltage drop across the electrodes is $V_d = I_d R_d$, where I_d is the total current flowing through the discharge region. The implications of the parallel resistance model will be discussed below.

C. Electron collision rates and excitation mechanisms

The mechanism by which the upper laser level, HgBr($B\,^2\Sigma_{1/2}^+$), is excited in an electric discharge has not, until recently, been definitively established. Early work by Schimitschek and Celto[1] suggested that HgBr(B) is created by electron impact dissociation of $HgBr_2$. However, a measure of this rate[16] yielded a cross section too small to account for the observed laser emission. Other mechanisms were suggested. Burnham[2] discovered that HgBr laser emission increased by the addition of N_2 to laser discharges consisting of $He/HgBr_2$. He speculated that the beneficial effect of nitrogen is not a result of excitation transfer from N_2 to HgBr(B) but rather a result of an increase in the quenching rate of the lower laser level due to dissociation of HgBr(X,v'') by N_2 ($v = 1$). In a later work, Nighan[12] suggested that in the absence of N_2 in the discharge, HgBr(B) is created by dissociative recombination of $HgBr_2^+$ to HgBr(B). The $HgBr_2^+$ results from Penning ionization of $HgBr_2$ by rare-gas atoms and by electron impact ionization of $HgBr_2$. In the presence of N_2, he suggested that HgBr(B) is additionally formed by dissociative excitation transfer following quenching of $N_2(A\,^3\Sigma_u^+)$ by $HgBr_2$. Chang and Burnham[17] measured this rate as well as the analogous rate for dissociative excitation by Xe ($^3P_2$). Brown and Nighan[5] added support for the Xe ($^3P_2$) excitation transfer mechanism by demonstrating superior laser efficiency in $Xe\text{-}HgBr_2$ mixtures as compared to $N_2\text{-}HgBr_2$ mixtures in an electron-beam-controlled discharge.

In later works, it became evident that the dominant excitation mechanism for HgBr(B) is by dissociative electron impact of $HgBr_2$. Nighan and Brown[13] presented a provisional set of excitation cross sections for this process, derived by matching model results to experimental gain and current density measurements. Experimentally measured ionization and dissociative attachment cross sections were also presented.[14] They grouped the electronic excitation of $HgBr_2$ into three processes having threshold energies of 5.0, 6.4, and 7.9 eV. The selection of these threshold energies was based, in part, on the electron energy loss spectra of Spence *et al.*[18] for electrons incident on $HgBr_2$. The first process results in dissociation of $HgBr_2$ to form ground-state HgBr($X\,^2\Sigma_{1/2}^+$) while the latter process results in excitation of a manifold of states of $HgBr_2$. The 6.4-eV process is the electron collision that results in dissociative excitation of HgBr(B), the upper laser level. A second set of semiempirical cross sections were presented by McGeoch *et al.*[15] who also grouped the excitation cross sections into 5.0-, 6.4-, and 7.9-eV processes in agreement with the energy loss spectra of Spence *et al.*[18] These works suggested that the electron impact dissociation of $HgBr_2$ resulting in HgBr(B) is a process having a peak cross section of approximately 1 A^2. A similar set of semiempirical cross sections, augmented by an experimental measurement of the laser excitation cross section, were developed by Kline *et al.*[19] This measured cross section[20] has a peak value of 3.2 A^2 at about 10 eV, maintaining that value for a plateau of at least another 10–20 eV. The peak value of this cross section is greater by a factor of 3 from those provisionally derived.[14,15] A second measurement of this cross section[21] yielded a peak value of only 0.75 A^2 at an electron energy of 9 eV, dropping to a plateau value of 0.4 A^2 at about 20 eV.

Although in qualitative agreement, the sets of semiempirical and experimental cross sections discussed above are in quantitative disagreement with regard to shape and peak values. To generate a set of cross sections for use in our kinetic model, we collated the works discussed above in the following manner. We used the experimentally measured cross sections for electron impact ionization of $HgBr_2$ (including branching ratios to $HgBr^+$) and for dissociative attachment as given by Nighan *et al.*[14] Their inferred cross sections for vibrational excitation of $HgBr_2$ were also used. The shape of the cross sections chosen for the 5- and 7.9-eV processes were similar to those of Kline *et al.*[19] Cross sections for excitation of HgBr(B) were selected similar to that of the experimental values of Malinin *et al.*[21] The magnitudes of these last three cross sections were adjusted until satisfactory agreement was obtained when compared to electron swarm data[14] and HgBr(B) fluorescence efficiency data.[15] The cross sec-

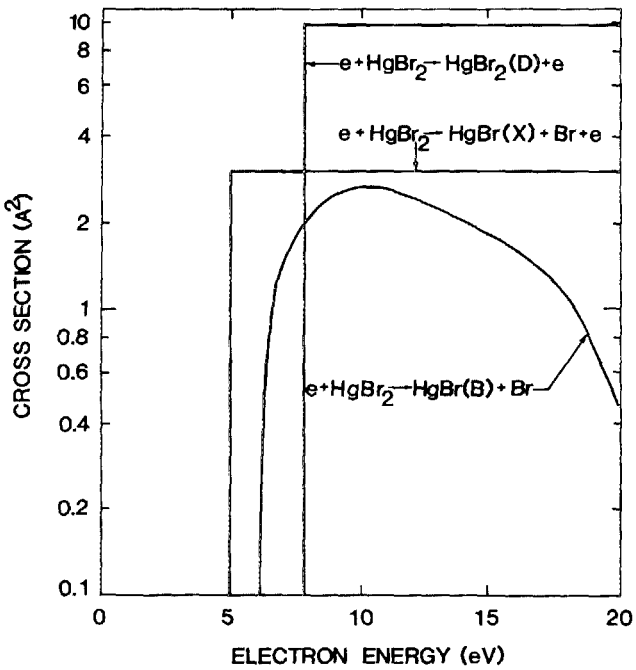

FIG. 3. Cross sections for the three electronic excitation processes of $HgBr_2$.

TABLE I. 6.4-eV Process cross section.

Energy (eV)	A^2	Energy (eV)	A^2
6.4	0.0	14.0	2.0
7.0	1.4	15.0	1.8
8.0	2.0	16.0	1.6
9.0	2.4	17.0	1.3
10.0	2.6	18.0	1.0
11.0	2.6	19.0	0.6
12.0	2.4	20.0	0.4
13.0	2.2	22.0	0.1

tions so obtained are plotted in Fig. 3. The 6.4-eV process cross section is listed in Table I.

Our set of derived cross sections differs from those previously discussed. The magnitude of the 7.9-eV process cross section is smaller by a factor of two from that of Nighan *et al.*[14] whereas the peak 6.4-eV process cross section is larger by approximately the same ratio. The 6.4-eV process cross section of Nighan *et al.* resembles a step function and that of McGeoch *et al.*, having a maximum value of 1.5 A^2 at 20 eV, decreases by only a factor of 2 at 100 eV. Our 6.4-eV process cross section is almost resonant in shape, decreasing sharply at 20 eV. This shape disagrees with the preliminary experimental results of Chen and Chantry.[20] Maintaining a plateau to the cross section, as do Nighan *et al.* and McGeoch *et al.*, overpredicted the value of laser pulse energy as compared to our experimental measurements when the PFN charging voltages were large. A part of this discrepancy may be due to an inadequate accounting in the model for the effects of constriction and parasitic discharge formation which are known to occur when large amounts of energy are deposited in the discharge. Constriction and parasitic discharge formation are discussed in Secs. IV and V.

Electron collision rate constants were obtained by solving Boltzmann's equation for the electron distribution function using the cross sections described above and those for the Ne buffer gas.[22] The electron distribution function was calculated with the computer code described in Ref. 23. Due to the expense of repeatedly generating the required electron collision rates, these values were parameterized as a function of E/N (electric field divided by number density) and fraction of $HgBr_2$ in Ne. A lookup table was generated with the results. Given the instantaneous value of E/N and fraction of $HgBr_2$, electron collision rates were obtained during execution of the computer code by performing a two-dimensional interpolation from this table. Using this method, the effects of electron-electron collisions on the electron distribution function and excitation rates are not self-consistently accounted for. This topic will be discussed in Sec. III. Rate constants for electron collisions with $HgBr_2$ for a 0.2% $HgBr_2$ in neon gas mixture are plotted in Fig. 4.

D. Other photon, heavy particle, and electron collision processes

Although the dominant mechanism for excitation of the upper laser level is electron impact dissociation of $HgBr_2$, the complete set of reactions is considerably more complicated. An abbreviated reaction scheme is sketched in Fig. 5. The species included in the model are listed in Table

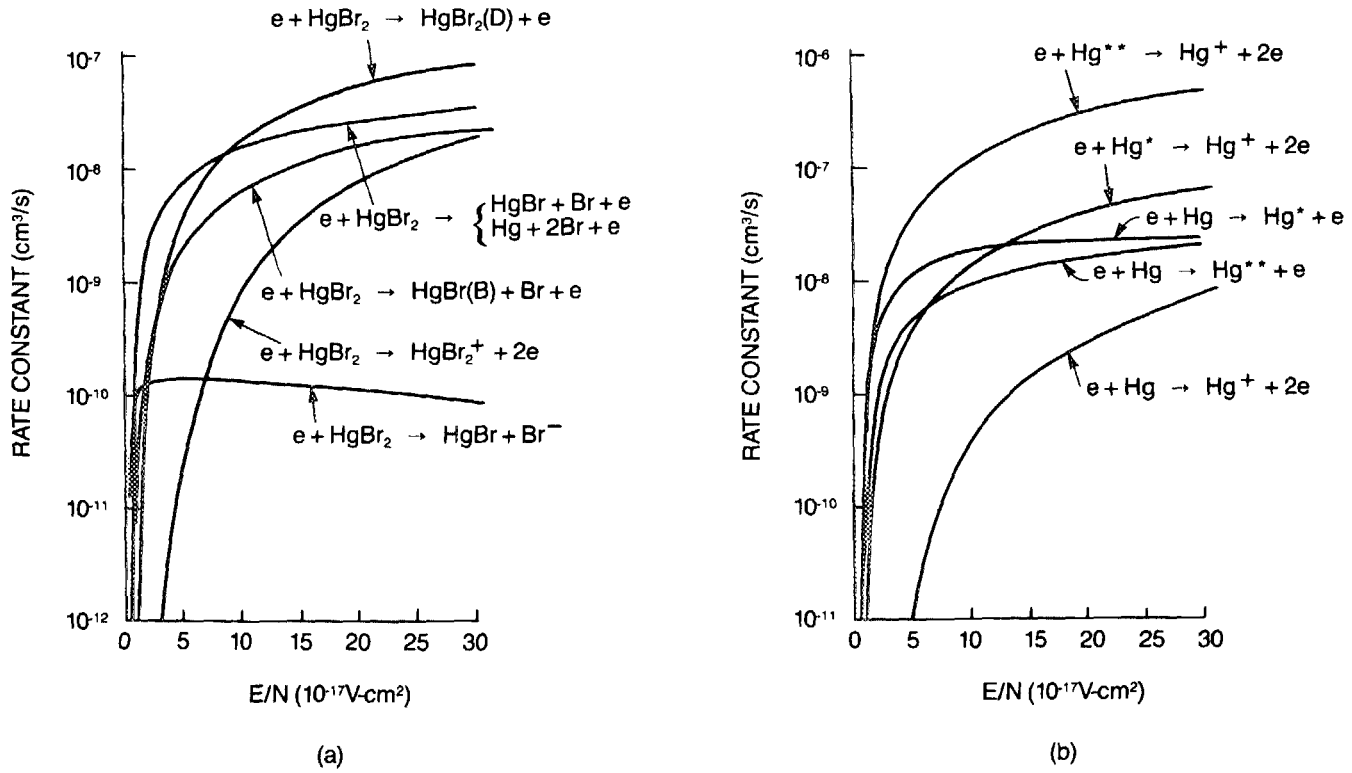

FIG. 4. Electron impact rate constants for excitation and ionization of (a) $HgBr_2$, and (b) $Hg(6\,^1S_0)$, Hg* ($6\,^3P_{1,0}$), and Hg** ($6\,^3P_2$). The gas mixture is 0.2% $HgBr_2$ in neon.

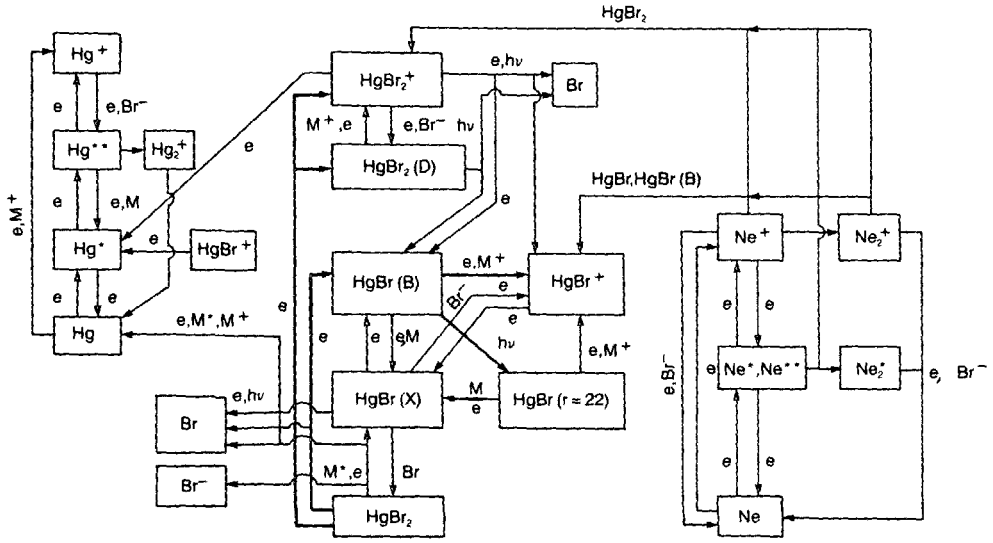

FIG. 5. Partial reaction scheme for electron impact and heavy particle collisions in $Ne/HgBr_2$ discharges. Since the time for reassociation of radicals to form $HgBr_2$ is long compared to the discharge pulse, the flow of energy in the diagram is from lower right to upper left, producing mercury ions as an end product.

II. In addition to those species listed in Table II, the gas temperature (T_g) and electron temperature (T_e) were also calculated. For non-Maxwellian electron distribution functions, we approximated $3/2\,kT_e = \epsilon$, where ϵ is the average electron energy obtained from solution of Boltzmann's equation. Note in the reaction scheme in Fig. 5 that the flow of energy is generally from lower right in the figure to upper left in the figure. The reassociation reactions for regeneration of $HgBr_2$ from radicals are too slow[24,25] to significantly replenish dissociated $HgBr_2$ during the 150-ns-long discharge pulse. Therefore, the flow of energy in the discharge results in the gradual reduction of $HgBr_2$ into Hg and Br. This direction of energy flow is responsible for much of the observed behavior in HgBr lasers.

Multistep processes are important in the reaction sequences that lead to forming ions other than Ne^+, particularly as applied to Hg* and Hg**. Electron impact ionization collisions from the excited states of mercury have the largest rate constants of any processes in the discharge. (See Fig. 4.) Therefore, reaction pathways that lead to formation of Hg, Hg*, or Hg** contribute heavily to the rate of ionization and subsequent impedance collapse of the discharge.[9] Atomic Hg is dominantly formed by direct electron impact dissociation of $HgBr_2$ in the 5.0-eV process, and to a lesser degree by dissociative Penning and charge exchange reactions of Ne*, Ne**, and Ne^+ with $HgBr_2(X)$, $HgBr_2(D)$, or HgBr(X,B). Hg* and Hg** are then produced rapidly by direct electron impact excitation of ground-state Hg, although Penning and charge exchange reactions of Ne*, Ne** and Ne^+ with $HgBr_2$ are sufficiently exothermic to produce Hg* as a primary product. In other multistep processes, $HgBr_2^+$ and $HgBr^+$ are readily formed by electron impact ionization of $HgBr_2(D)$ and HgBr(B), and by Penning ionization and charge exchange of $HgBr_2$ with Ne*, Ne**, and Ne^+.

TABLE II. Species included in the model.

e	Electrons	$HgBr_2(X)$	Ground state
Ne	Ground-state neon	$HgBr_2(D)$	7.9-eV process
Ne*	Ne(3^3P)	$HgBr_2^+$	
Ne**	Pseudostate (18.6 eV)	HgBr(X)	Ground state
Ne^+		HgBr(X,$v = 22$)	Lower laser level
Ne_2^*		HgBr(B)	Upper laser level
Ne_2^+		$HgBr^+$	
Hg	Ground state ($6\,^1S_0$)	Br	
Hg*	Hg($6\,^3P_{1,0}$)	Br^-	
Hg**	Hg($6\,^3P_2$)		
Hg^+			
Hg_2^+			

Electron impact rates and heavy particle reaction rates used in the model are listed in Table III. All of these variables are computed as a function of time and position in the discharge.

The laser photon extraction model is a self-consistent Rigrod analysis[39] as modified by Reuven and Baer[40] to account for longitudinal effects. Of the laser intensity calculated for each vertical region of the discharge, only a fraction is considered as laser output intensity. This value is the fractional area overlap of the circular optics with the area of the particular region (see Fig. 2).

Although the time scales of interest are too short for convection of the gas caused by gas heating to be important (see Sec. IV), gas heating may be important with respect to the change in kinetic rates, which are proportional to $T_g^{1/2}$. Therefore, the gas temperature was included as a variable in the model. The time rate of change of gas temperature was calculated according to

$$\frac{\partial}{\partial t}(\rho c_p T_g) = \tfrac{3}{2} n_e k \left(T_e - T_g\right) \sum_i \nu_i \left(\frac{2m}{M_i}\right) + \nabla \lambda \nabla T_g, \tag{18}$$

where ρ is the gas density, c_p is the specific heat, ν_i is the electron collision frequency, m is the electron mass, M_i is the heavy particle mass, and the summation is over heavy species in the discharge. The last term, in which λ is the thermal conductivity of the gas, is for thermal conduction. On our time scales (a few hundred nanoseconds), thermal conduction does not make a significant contribution to the change in gas temperature. The typical increase in gas temperature during a single discharge pulse is 25–50 °K on a volume aver-

TABLE III. Rates for electron impact and heavy particle collisions, and photon processes.

Process	Rate*	Reference
Electron impact excitation, quenching attachment, and ionization		
$e + HgBr_2 \rightarrow HgBr + Br + e$ (0.6)		
$\rightarrow Hg + 2Br + e$ (0.4)	(a)	(30)
$\rightarrow HgBr(B) + Br + e$	(a)	
$\rightarrow HgBr_2(D) + e$	(a)	
$\rightarrow HgBr_2^+ + 2e$	(a)	
$\rightarrow HgBr^+ + Br + 2e$	(a)	
$\rightarrow HgBr + Br^-$	(a)	
$e + HgBr_2(D) \rightarrow HgBr_2^+ + 2e$	$\epsilon = 2.7$ eV (c)	
$e + HgBr_2^+ \rightarrow HgBr(B) + Br(0.2)$		
$\rightarrow HgBr + Br$ (0.8)	$2.0(-7)/T_e^{0.5}$(d)	(12)
$e + HgBr(v = 22) \rightarrow HgBr + e$	2.0(−9) (d,g)	
$e \rightarrow HgBr \rightarrow HgBr(B) + e$	$\epsilon = 2.9$ eV(c)	
$\rightarrow HgBr^+ + 2e$	$\epsilon = 8$ eV(c)	
$\rightarrow Hg + Br + e$	$\epsilon = 5$ eV (e)	
$\rightarrow Hg + Br^-$	1.0(−11)(d)	
$e + HgBr(B) \rightarrow HgBr^+ + 2e$	$\epsilon = 5.1$ eV(c)	
$\rightarrow HgBr + e$	1.0(−8)(d)	
$e + Hg \rightarrow Hg^*(6\,^3P_{0,1}) + e$	(b,g)	(35)
$\rightarrow Hg^{**}(6\,^3P_2) + e$	(b,g)	(35)
$\rightarrow Hg^+ + 2e$	(b)	(35)
$e + Hg^* \rightarrow Hg^{**} + e$	(b,g)	(36)
$e + (Hg^*, Hg^{**}) \rightarrow Hg^+ + 2e$	(b)	(37)
$e + Ne \rightarrow Ne^* + e$	(b,g)	(22)
$\rightarrow Ne^{**} + e$	$\epsilon = 18.6$ eV (c)	
$\rightarrow Ne^+ + 2e$	(b)	(22)
$e + Ne^* \rightarrow Ne^{**} + e$	$\epsilon = 2.0$ eV (c,g)	
$\rightarrow Ne^+ + 2e$	$\epsilon = 5.0$ eV (e)	
$e + Ne^{**} \rightarrow Ne^+ + 2e$	$\epsilon = 3.0$ eV (c)	
$e + Br^- \rightarrow Br + 2e$	(f,h)	
Electron-ion recombination		
$e + HgBr^+ \rightarrow Hg^* + Br$	1.0(−7) (d)	(12)
$e + Ne_2^+ \rightarrow Ne^* + Ne(0.9)$		
$\rightarrow Ne^{**} + Ne(0.1)$	1.(−7)	(26)
$e + Hg^+ \rightarrow Hg^{**}$	$1.0(-11)/T_e^{0.5}$ (d)	(34)
Ion-ion neutralization		
$Br^- + Hg^+ \rightarrow Hg^* + Br$	1.0(−8) (d)	
$Br^- + HgBr_2^+ \rightarrow HgBr(B) + 2Br(0.2)$		
$\rightarrow HgBr + 2Br(0.8)$	1.0(−8) (d)	
$Br^- + HgBr^+ \rightarrow HgBr(B) + Br(0.2)$		
$\rightarrow HgBr + Br$ (0.8)	1.0(−8) (d)	
$Br^- + Ne^+ \rightarrow Ne + Br$	1.0(−8) (d)	
Photon processes		
$h\nu(502\text{ nm}) + HgBr(B) \rightarrow HgBr(v = 22) + 2h\nu(502\text{ nm})$	$1.5(-16)$ cm^2	(3)
$h\nu(502\text{ nm}) + HgBr_2^+ \rightarrow HgBr^+ + Br$	$2.0(-18)$ cm^2	(24)
$h\nu(502\text{ nm}) + HgBr^+ \rightarrow Hg^+ + Br$	$2.0(-18)$ cm^2(d)	
$h\nu(502\text{ nm}) + HgBr \rightarrow Hg + Br$	$1.0(-19)$ cm^2 (d)	
$HgBr(B) \rightarrow HgBr(v = 22) + h\nu(502\text{ nm})$	4.3(7) s^{-1}	(30)
$Ne_2^* \rightarrow 2Ne + h\nu$	7.5(7) s^{-1}	(27)
Heavy particle quenching		
$HgBr_2(D) + Ne \rightarrow HgBr + Br + Ne$	$5.3(-13)$ (d)	(29)
$HgBr_2(D) + HgBr_2 \rightarrow HgBr + Br + HgBr_2$	$1.7(-10)$ (d)	(29)
$HgBr(B) + Ne \rightarrow HgBr + Ne$	$5.0(-13)$	(29)
$HgBr(B) + HgBr(B) \rightarrow 2HgBr$	$2.0(-11)$ (d)	
$HgBr(B) + HgBr_2 \rightarrow HgBr + HgBr_2$	$1.7(-10)$	(29)
$HgBr(v = 22) + Ne \rightarrow HgBr + Ne$	$6.0(-12)$	(24,31)
$Ne^{**} + Ne \rightarrow Ne^* + Ne$	$5.0(-11)$	(27)
$Hg^{**} + HgBr_2 \rightarrow Hg^* + HgBr_2$	$2.0(-10)$	(38)

TABLE III. continued

Process	Rate*	Reference
$HgBr/HgBr_2$ reassociation		
$HgBr + Br + Ne \rightarrow HgBr_2 + Ne$	1.0(− 32) cm^6/s (d)	(32,33)
$Hg + Br + Ne \rightarrow HgBr + Ne$	1.0(− 32) cm^6/s (d)	(32,33)
Excitation transfer, charge exchange, and ion-molecule reactions		
$Ne^+ + 2Ne \rightarrow Ne_2^+ + Ne$	4.4(− 32) cm^6/s	(28)
$Hg^* + HgBr_2 \rightarrow Hg + HgBr + Br$(0.42)		
$\rightarrow 2HgBr$ (0.58)	2.0(− 10) (d)	
$Ne^* + HgBr_2 \rightarrow Hg^{**} + Ne + 2Br$	1.0(− 10) (d)	
$\rightarrow HgBr + Ne + Br$	1.0(− 14) (d)	
$\rightarrow HgBr_2^+ + Ne + e$	1.0(− 10) (d)	
$Ne^{**} + HgBr_2 \rightarrow HgBr(B) + Ne + Br$	1.0(− 14) (d)	
$\rightarrow HgBr + Ne + Br$	1.0(− 14) (d)	
$\rightarrow HgBr_2^+ + Ne + e$	2.4(− 10) (d)	
$Ne^+ + HgBr_2 \rightarrow HgBr_2^+ + Ne$	6.0(− 11) (d)	
$HgBr_2^+ + Hg \rightarrow HgBr_2 + Hg^+$	2.0(− 10) (d)	
$HgBr_2(D) + Hg \rightarrow Hg^{**} + HgBr_2$	2.0(− 10) (d)	
$Hg^* + Hg^* \rightarrow Hg_2^+ + e$	5.0(− 10) (d)	
$Ne^* + M \rightarrow M^+ + Ne + e$	6.0(− 11) (d)	
$Ne^{**} + M \rightarrow M^+ + Ne + e$	6.0(− 11) (d)	
$Ne^+ + M \rightarrow M^+ + Ne$	6.0(− 11) (d)	
[M = HgBr, HgBr($v = 22$), HgBr(B),$HgBr_2(D)$]		
$Ne^* + 2Ne \rightarrow Ne_2^* + Ne$	4.0(− 34) cm^6/s	(27)

*Rate constants are in units of cm^3/s unless noted otherwise.
Notation: "8.5(− 8) (d)" denotes 8.5×10^{-8}, refer to footnote (d).

[a] Rate is obtained as a function of E/N by solution of Boltzmann's equation for the electron distribution function. Cross section is in Fig. 3. Examples of rates are in Fig. 4.

[b] Rate is obtained as a function of E/N by solution of Boltzmann's equation for the electron distribution function. Cross sections are contained in listed reference.

[c] Rate is approximated. Form of approximation is using analytic expression for electron impact rates for Maxwellian electron distributions.[47] Rate is a function of threshold energy of the process and average electron energy. The threshold energy ϵ is indicated. The average electron energy is obtained from the solution of Boltzmann's equation.

[d] Rate is estimated. See indicated reference for similar reactions.

[e] Rate is 0.01 times the rate calculated in the fashion for footnote (c).

[f] Rate is a function of electron temperature as given in indicated reference. The electron temperature is approximated from average electron energy obtained from solution of Boltzmann's equation.

[g] Reverse reaction is also included. Reverse rate is obtained from detailed balancing.

[h] Cross section is a 5 A^2 step function with threshold energy of 3.36 eV.

aged basis and $\geqslant 100$ °K in the constricted core of the discharge.

Diffusion of neutral species is not important on our time scales and is not included in the model. Diffusion of charged species, though, may be important and we used the ambipolar diffusion approximation to describe it. In the ambipolar diffusion approximation, the rate of diffusion of positive ions is assumed to be equal to that of electrons and negative ions.[41] The magnitude of the ambipolar electric field E is obtained by equating the rate of diffusion of negative and positive charge carriers:

$$E = -\frac{D_e \nabla N_e + D_I^- \nabla N_I^- - D_I^+ \nabla N_I^+}{(\mu_e N_e + \mu_I^- N_I^- + \mu_I^+ N_I^+)}. \quad (19)$$

In Eq. (19), D is a free diffusion constant, N is a charged particle density, and μ is a mobility. The subscripts e and I refer to electrons and ions, respectively, and the superscripts $-$ and $+$ refer to negative and positive ions. Given this value for the ambipolar electric field, we add to the time rate of change of the charged species,

$$\frac{\partial N}{\partial t} = -\nabla D \nabla N \pm \nabla \mu N E. \quad (20)$$

During a 200-ns-long discharge pulse, the change in the number density of charged particles due to ambipolar diffusion is only about 0.1% of the total. This effect is therefore not important unless electrons diffuse into and subsequently avalanche in a region that was not preionized.

III. COMPARISON OF MODEL RESULTS WITH EXPERIMENTAL DATA, AND TYPICAL TIME AND SPATIAL DEPENDENCE OF LASER INTENSITY AND CURRENT DENSITY

For purposes of discussion and comparing results of the model to experimental data, we chose operating conditions corresponding to those of our solid dielectric PFL HgBr laser. This device has a maximum laser pulse energy of 3.2 J and is preionized by x rays to an electron density of about 5×10^8 cm^{-3}.[11] The typical operating temperature is 450 °K and the gas mixture is ≈ 7 Torr of $HgBr_2$ in 5 atm of neon. The nominal discharge dimensions and circuit values are as given in the introduction to Sec. II and in Sec. II A. The length of the discharge electrodes is 100 cm and the mid-electrode spacing is 6.5 cm. The discharge region is 4–6 cm wide, a width determined by masking of the preionizing x

rays. The laser cavity consists of a total reflector and a 20% reflector as an output coupler. The distance between the mirrors is 160 cm.

Typical experimental and computed waveforms for voltage, current, laser intensity, and sidelight fluorescence are shown in Figs. 6 and 7. Qualitatively, there is good agreement. Good agreement is obtained between experiment and theory for the peak breakdown voltage, self-sustaining voltage and the peak current. The experimental voltage waveform falls more quickly from its maximum value and collapses somewhat faster than the computed waveform. This behavior is reflected in the current, laser, and fluorescence waveforms. The experimental current waveform rises more quickly than does the computed waveform and the laser turns on more quickly. The experimental fluorescence waveform maintains a plateau after threshold for only a short time before rapidly decreasing. The computed fluorescence waveform maintains a plateau appearance for the duration of the laser pulse. The experimental waveforms indicate a more rapid breakdown and more severe impedance collapse than accounted for in these calculations. There are two dominant causes for impedance collapse in the HgBr laser.

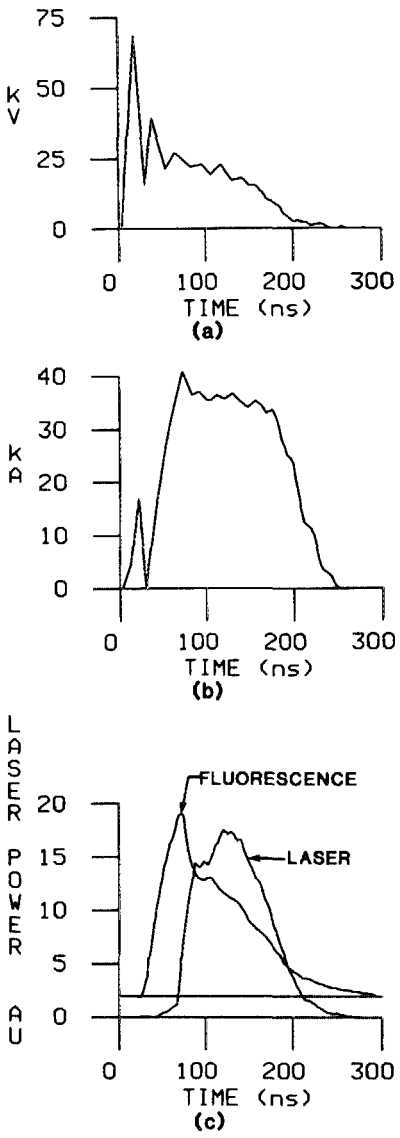

FIG. 6. Typical experimental waveforms: (a) voltage (kV); (b) current (kA); (c) laser power and sidelight fluorescence (arbitrary units).

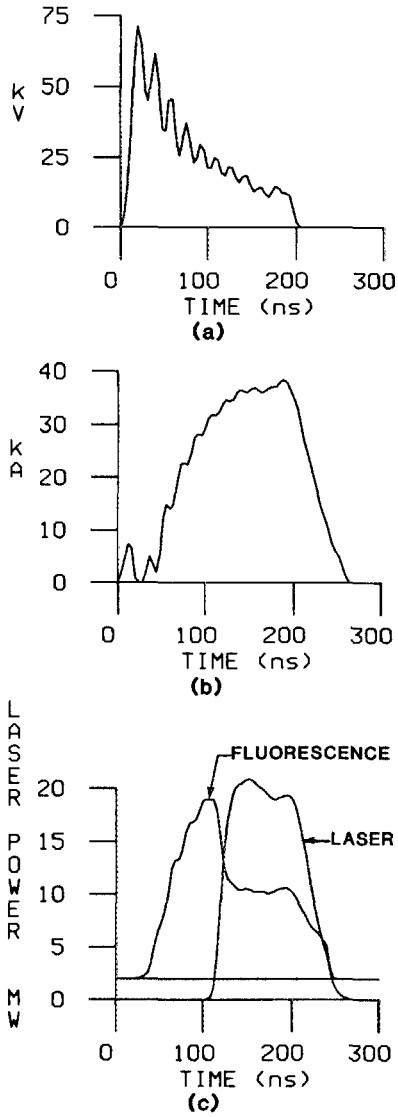

FIG. 7. Typical computed waveforms for the conditions of Fig. 6: (a) voltage (kV); (b) current (kA); (c) laser power (MW) and sidelight fluorescence (arbitrary units).

The first, which may not necessarily reduce the total laser pulse energy, is constriction of the discharge. The second is parasitic discharge losses. A parasitic discharge is defined as a discharge path through the gas, not within the optical cavity, which reduces laser pulse energy. Both of these effects will be discussed below.

Typical time and spatial dependence for laser intensity and current density in the HgBr laser are plotted in Fig. 8. The shape of the electrodes, the preionization density profile, and the plane of observation are also indicated. Note that the current density, initially relatively uniform as a function of position, tends to constrict fairly rapidly towards the axis. This trend is reflected in the shape of the laser pulse. The laser intensity is initially uniform, reaching threshold first near the axis and slowly spreading out towards the edges. When the discharge begins to constrict, the laser intensity quickly collapses towards the axis.

The collapse of the discharge is more evident in the time and spatial dependence of the density of HgBr(B) plotted in Fig. 9 for the same conditions as Fig. 8. The onset of laser oscillation is denoted by the rapid decrease in upper laser level density, an indication of the transition being saturated by the laser intensity. This event occurs first on the axis and

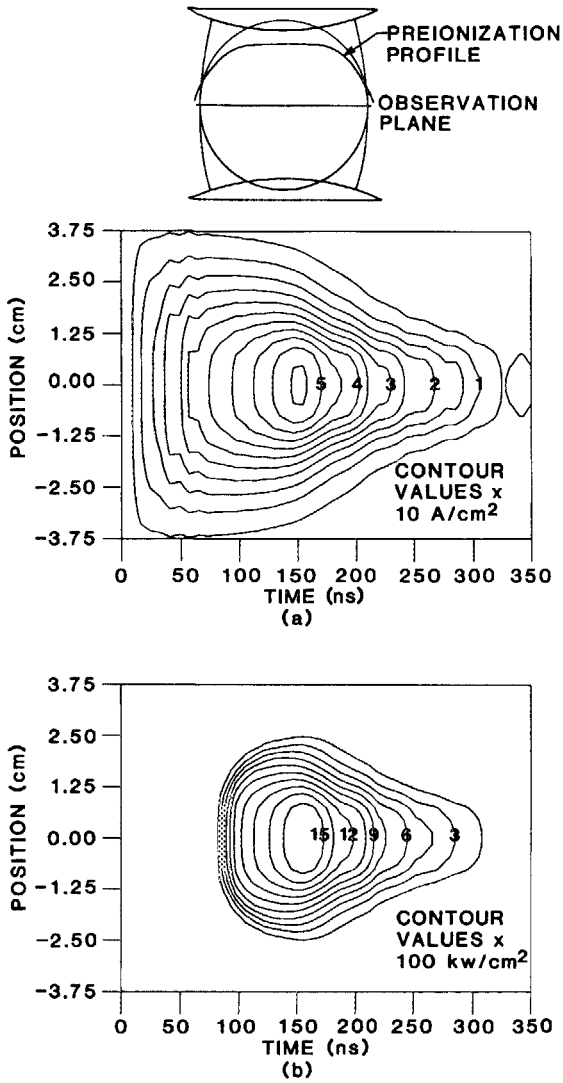

FIG. 8. Typical computed time and spatial dependence for (a) current density and (b) laser intensity. The contour labels are in units of 10 A/cm^2 and 100 kW/cm^2. The interelectrode gap spacing is 6.5 cm and the electrode length is 100 cm. The PFN is charged to 58 kV and stores 125 J. The plane of observation for the plots and the preionization electron density profile (peak value 5×10^9) are indicated in the center diagram.

propagates outwards. The outer limit of laser oscillation is indicated by the absence of saturation of the upper laser level. Note that the threshold value of HgBr(B) decreases from the axis to the edge of the discharge. This trend results from higher absorption losses near the axis. Also on the axis there is a larger "overshoot" of HgBr(B) density beyond the threshold value than at the edge. This results from the finite buildup time required for the laser intensity once the inversion is obtained. The increase in upper laser level density on the axis after threshold also indicates an increase in the pumping rate as a result of discharge constriction and increased losses to absorption by ions. For these conditions the density of $HgBr_2$ on the axis is reduced to a value of only 73% of the initial value. When current constriction and depletion of $HgBr_2$ are limited to these values, the increase in pumping rate to the upper laser level in the constricted region is sufficient to offset the reduction in the cross-sectional area in which the laser is oscillating. As a result, the total laser energy and efficiency do not suffer. This is not the case when the profile of the preionization electron density is not uniform or the discharge is operated with large energy loading. These aspects of discharge stability will be discussed below.

Experimental and computed laser energy as a function of stored energy on the PFL (or PFN) are plotted in Fig. 10. The impedance and length of the PFL/PFN are constant. Stored energy is increased by increasing the charging voltage. Also indicated in Fig. 10 is laser efficiency, defined as (laser energy)/(stored electrical energy). Laser energy increases with increasing stored energy but with a decreasing efficiency. The maximum experimental efficiency of 2.2% occurs at a stored energy of 115 J. The calculation yields a similar efficiency, but it occurs at about 130 J. The dependence of laser efficiency on stored energy is different for different values of the impedance of the PFL/PFN and of the initial $HgBr_2$ density. For constant PFL/PFN impedance and a fixed initial density of $HgBr_2$, laser efficiency decreases with increasing stored energy as a result of three dominant mechanisms: discharge constriction, geometrically dependent depletion of $HgBr_2$, and parasitic discharge losses. Model results for laser efficiency are overestimated in Fig. 10 for large stored energy in part due to the exclusion of parasitic discharges in the calculation. Details of this effect are sensitive functions of geometrical factors such as electrode shapes and electric field enhancement at sharp edges. The dependance of laser efficiency on the preionization electron density is in part due to this effect and will be discussed in Sec. V.

The electron density corresponding to the maximum current density in Fig. 8 is 1.0×10^{14} cm^{-3}, yielding a fractional ionization of $\simeq1.5\times10^{-6}$. At this level of fractional ionization, electron-electron (e-e) collisions can have a signif-

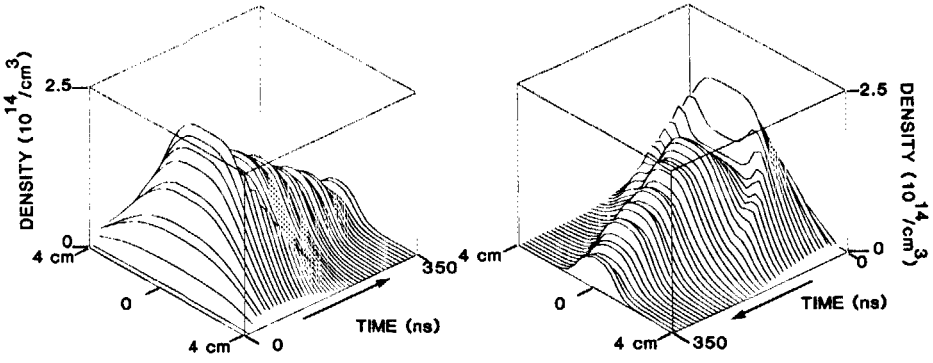

FIG. 9. Computed density of HgBr(B) for the conditions of Fig. 8. The two figures are of the same data, however time is plotted in opposite directions. The onset of laser oscillation is indicated by the rapid saturation of the upper laser level.

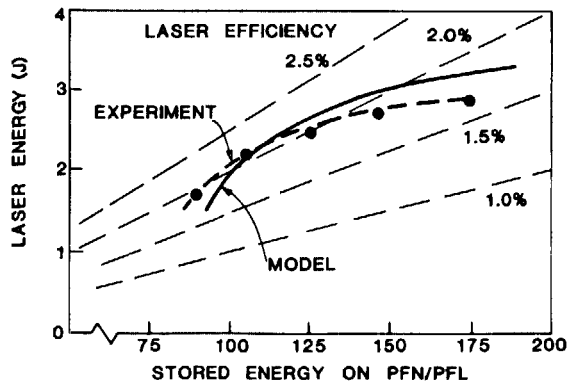

FIG. 10. Experimental and computed laser pulse energy as a function of stored energy on the PFL/PFN. The dotted lines indicate the loci of constant efficiency. Efficiency decreases with increasing stored energy due to current constriction, progressive impedance mismatch, and depletion of $HgBr_2$.

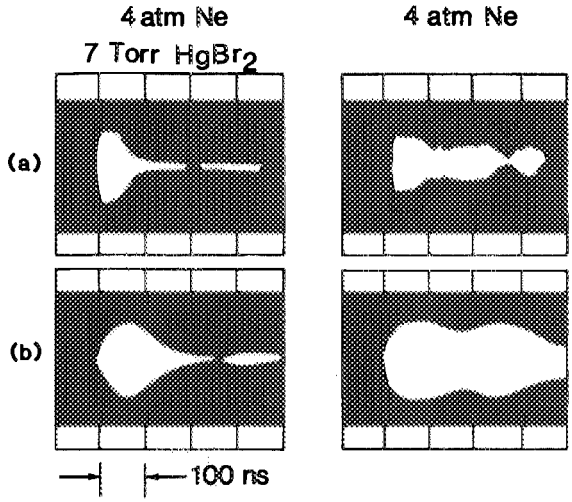

FIG. 11. Streak camera photographs of fluorescence from $HgBr_2$/Ne and Ne discharges: (a) experiment and (b) simulation for similar conditions. The simulation is the contour corresponding to approximately 5% of the instantaneous maximum current density. Note the current constriction and ringing of the discharge for the $HgBr_2$/Ne mixture. The Ne discharge does not constrict, even over many PFL/PFN periods.

icant influence on electron collision rates. The effect of *e-e* collisions is to drive the electron distribution function towards a Maxwellian and therefore increase electron collision rates having high threshold energies (e.g., ionization) as compared to those with low threshold energies (e.g., vibrational excitation). The exclusion of *e-e* collisions in our analysis therefore deemphasized the contribution of ionization from ground states, and excitation of HgBr(D), Ne*, and Ne**. Multistep processes, which are a sequence of relatively low threshold energy collisions, are less effected by the exclusion of *e-e* collisions. The rate of impedance collapse predicted by the model during times when multistep processes are not yet important therefore may be too small due to the absence of *e-e* collisions in the analysis. This might in part explain the discrepancy between theory and experiment shown in Figs. 6 and 7. The exclusion of *e-e* collisions is less important late in the discharge when multistep processes begin to dominate, and when experiment and theory are in better agreement.

IV. CURRENT CONSTRICTION AND IMPEDANCE MATCHING IN HgBr LASERS

The degree to which constriction of the discharge occurs, and is subsequently detrimental to laser efficiency, is a function of a number of factors: preionization electron density profile, electrode contours, length of the discharge pulse, $HgBr_2$ density, and power loading. The extent to which $HgBr_2$, and its dissociation products, contribute to the constriction process is illustrated in Fig. 11. In this figure are streak camera photographs of fluorescence from a discharge in a mixture of 7-Torr $HgBr_2$ in 4 atm of neon, and from a discharge in 4-atm neon only.[10] Simulated streak camera photographs are the contours of the current density corresponding to $\approx 5\%$ of the instantaneous maximum value. In the $HgBr_2$/Ne discharge, constriction occurs quite rapidly. Upon reflection of the voltage at the termination of the PFL, the discharge "relights" only on the axis. This is indicated in both the experiment and simulation by the thin line of fluorescence (or current density) on the axis for times greater than 150 ns. In the Ne discharge, though, the discharge width remains at a large fraction of its initial value for many PFL voltage reflections. Some portion of this effect is due to better impedance matching to the PFL with the $HgBr_2$/Ne discharge, which results in a larger fraction of the stored energy being delivered to the discharge during the first voltage transit. The dominant cause, though, is constriction of the discharge. The mechanisms for current constriction in discharges typical of HgBr lasers will now be discussed.

The constriction we have discussed thus far is not due to changes in gas density caused by diffusion or convection, as can be seen from the following arguments. Consider a continuous longitudinal glow discharge in a round tube. The electron density will initially assume a profile approximately given by $n_{e0}J_0(r/R_1)$, where n_{e0} is the on-axis electron density, J_0 is the zero-order Bessel function, and R_1 is its first zero. The gas is heated by electron collisions in the bulk and cooled by conduction to the wall. With a higher electron density on the axis of the discharge, the rate of gas heating is higher there. As the gas temperature on the axis of the discharge increases relative to that near the wall, the gas density decreases on the axis as a result of diffusion or convection. The lower gas density on the axis allows a higher E/N which results in a higher electron and current density and a higher rate of gas heating. The higher rate of heating increases the gas temperature on the axis, thereby reducing the gas density, and so on. The process is often unstable, and when it leads to constriction, the discharge is called thermally unstable.

In order for the sequence of events described above to lead to a thermal instability and constriction of a discharge, the total duration of the discharge must be long compared with the time required for convection (or diffusion) of the gas to create a region of rarified gas density. This time is approximately $\Delta t = l(3V\rho/E)^{1/2}$ where l is the scale length, ρ is the gas density, V is the volume of the discharge, and E is the energy deposited in the discharge. For our parameters ($E = 100$ J, $V = 2400$ cm^3, $l = 0.2$ cm, $\rho = 0.003$ g/cm^3), $\Delta t \approx 30$ μs, which is long compared to the duration of the

discharge ($\approx$200 ns). Therefore, constriction of the discharge does not result from convection of the gas, but rather occurs as a result of some spatially nonuniform initial condition (e.g., preionization electron density profile, $HgBr_2$ density) or ionization rates that are spatially varying resulting from a nonuniform electric field. This condition is also known as an ionization instability. The degree of constriction and magnitude of the ionization instability also depends on the duration and the rate of energy deposition.

A. Rate of energy deposition

The degree to which the rate and duration of energy deposition in the discharge can lead to constriction is illustrated in Fig. 12. The electrode shape and preionization electron density are the same as in Fig. 8. In Fig. 12(a), current density for our nominal operating conditions is plotted ($\tau = 145$ ns, $V_0 = 58$ kV). In Fig. 12(b), current density is plotted for a PFN of the same time duration but with twice the stored energy ($V_0 = 82$ kV) such that the rate of energy deposition is approximately doubled. Finally, in Fig. 12(c), the PFN voltage remains at 58 kV; however, the line length and, hence, stored energy are doubled. The rate of energy deposition is approximately the same as in Fig. 12(a), but the duration of deposition is twice as long. For the latter two cases, the discharge constricts after a critical amount of energy is deposited in the gas. The constriction is severe enough that the impedance of the discharge changes to the point that impedance matching with the PFN can no longer be maintained. The impedance mismatch is indicated by the voltage reflection at the end of the PFN and the "relighting" of the discharge. Impedance matching in the HgBr laser is discussed in more detail below.

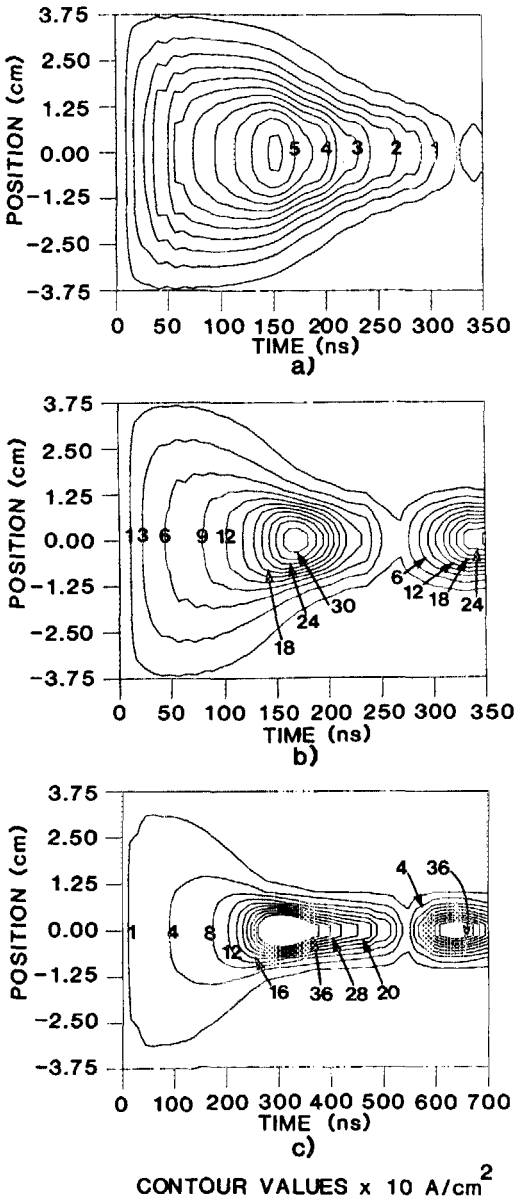

FIG. 12. Current density in $HgBr_2$/Ne discharges computed for different rates and duration of energy deposition: (a) nominal case with stored energy on PFN of 125 J and PFN length of 125 ns; (b) stored energy on PFN of 250 J and PFN length of 125 ns, thereby doubling the rate of energy deposition from (a); (c) stored energy on PFN of 250 J and PFN line length of 250 ns, thereby doubling the duration of energy deposition from (a). The contour labels are in units of 10 A/cm^2. Note the change in time scale for (c).

B. Electrode contours

Discharge lasers that operate efficiently have electrode contours that maximize the uniformity of the plasma, presumably by maximizing the uniformity of the applied electric field.[42] Electrode contours that cause a particular discharge region to have an electric field larger than the average value can promote constriction of the discharge. Electrodes having surface imperfections with sharp edges may have sufficient enhancement of the local electric field that discharge streamers result.[43]

We examined the sensitivity of the HgBr laser to changes in the contours of the electrodes with our model. For this exercise, the electron preionization density profile, circuit conditions, and midgap spacing remained constant. Only the thickness of the electrode (distance h in Fig. 2) was changed, thereby changing the curvature of the electrodes. Electrode shapes and resulting laser pulses for three variations in electrode contours are plotted in Fig. 13. Clearly, the more severely curved electrodes result in more severely constricted laser pulses. However, the total laser pulse energy does not decrease as a consequence of the constriction. The spatial uniformity of the laser intensity, though, clearly suffers. For these examples, laser pulse energy actually increases for the more severely curved electrodes. The reason for this trend is that the increased pump rate to the upper laser level in the constricted region is larger than the decrease in cross-sectional area. This indicates that $HgBr_2$ is not being severely depleted in these examples. Note that laser threshold occurs first on the axis and spreads towards the periphery for the severely curved electrodes, whereas laser threshold is obtained almost simultaneously across the plane of observation for the flatter electrodes. The total time duration of the current pulse increases as the curvature of the electrodes increases. This results from a progressively larger impedance mismatch of the discharge to the PFN as the plasma begins to constrict. The flattest electrodes in our examples result in a discharge that is well impedance matched to the PFN, thereby resulting in a crisp, square current, and laser pulse.

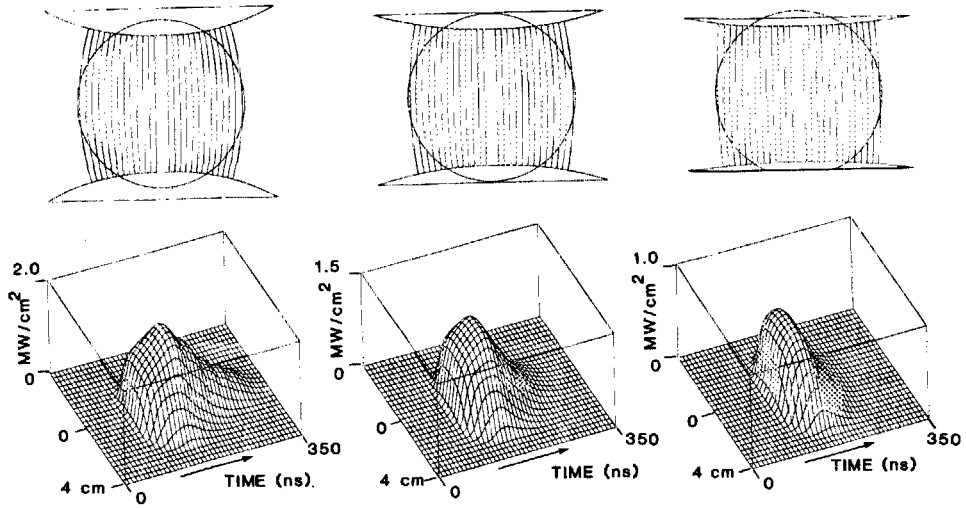

FIG. 13. Laser intensity as computed for different electrode contours. The electrode contours for each example are shown above the plot of laser intensity and are progressively less curved from left to right. Although constriction of the discharge occurs with severely curved electrodes, for these conditions laser pulse energy does not decrease because $HgBr_2$ is not being depleted. Flatter electrodes, without constriction, provide a better impedance match to the PFN.

C. Preionization electron density profile

The influence of the contour of the electrodes on the stability of the discharge is manifested through the local value of E/N. If, as a result of the shape of the electrodes, the local value of E/N is significantly different at one location in the discharge with respect to another, then excitation and ionization rates also will be different. The degree to which the spatially dependent excitation rates result in one region of the discharge becoming more conductive than another and, hence, leading to constriction depends on the magnitude of the difference between the local values of E/N.

For the conditions where E/N is uniform throughout the discharge region and in the absence of surface flaws on the electrodes, the stability of the discharge then becomes a

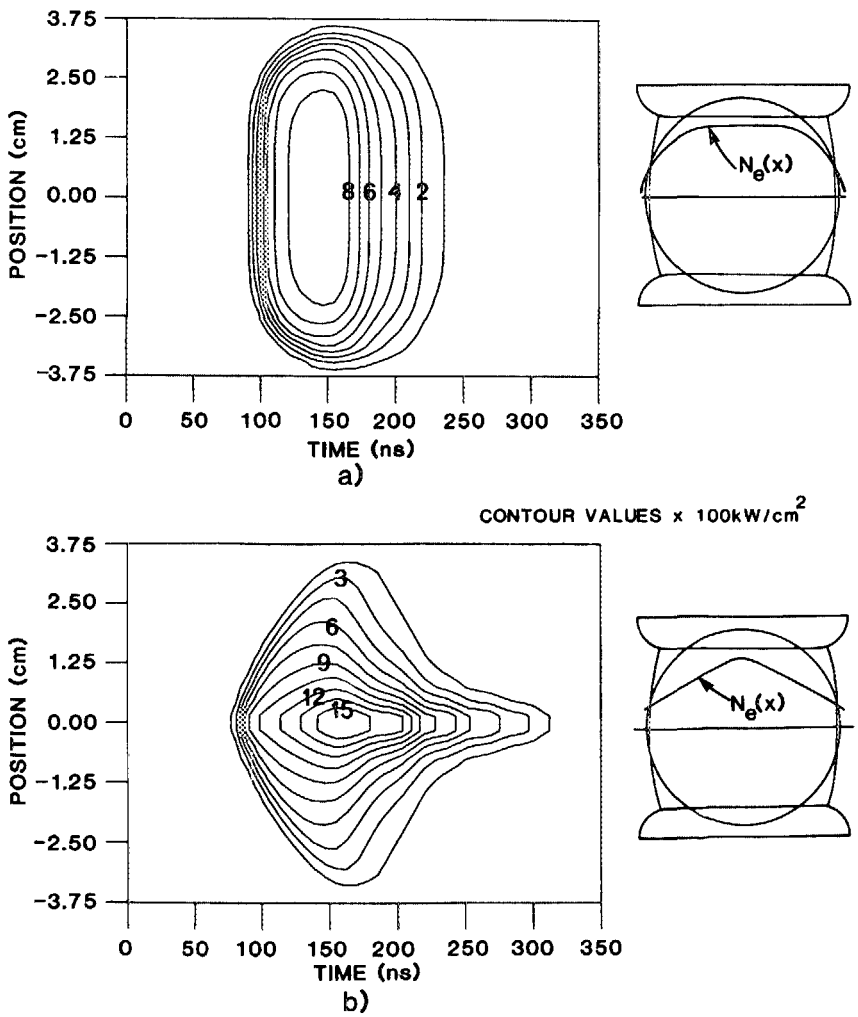

FIG. 14. Model results for laser intensity as a function of preionization electron density profile: (a) uniform profile and (b) nonuniform profile. The electrodes are flat in each case and the preionization electron density profile is indicated in the diagram at the right of each figure. The contour labels are in units of 100 kW/cm². A preionization electron density profile peaked on the axis results in multistep processes becoming the dominant ionization mechanism at an earlier time at that location, thereby promoting constriction of the discharge.

function solely of the preionization electron density profile. If the preionization electron density profile is also uniform throughout the discharge region, one would in turn expect the current density and laser flux to be uniform also. In practice, though, the preionization electron density profile is not uniform and, as a consequence, constriction of the discharge occurs. The rapidity with which this constriction can occur, in spite of excitation rates being similar, is a result of stepwise ionization. We consider this effect below.

Laser intensity for discharges with flat electrodes, but with uniform and nonuniform preionization density profiles, is plotted in Fig. 14. Clearly, the case with a nonuniform electron density rapidly leads to constriction and subsequent impedance mismatch to the PFN. The case of uniform preionization density has a current and laser pulse with a duration equal to that of the length of the PFN, indicating a good impedance match. X-ray preionization devices having line sources, as opposed to broad sources, have a highly divergent output of x rays and produce a relatively nonuniform preionization electron density profile. The use of preionizers with line sources therefore are more likely to result in discharges that suffer from constriction than preionizers having broad sources.

The extent to which multistep ionization is responsible for current constriction when the preionization electron density is not uniform is illustrated in Fig. 15. In this figure, the increase in current density due to multistep processes is plotted for the nonuniform preionization electron density profile of Fig. 14. The plot in Fig. 15 was generated by recomputing the previous example while excluding multistep ionization processes and subtracting the respective current densities. The increase in current density on the axis indicates the importance of multistep ionization with respect to discharge stability, a topic treated in more detail in the next section.

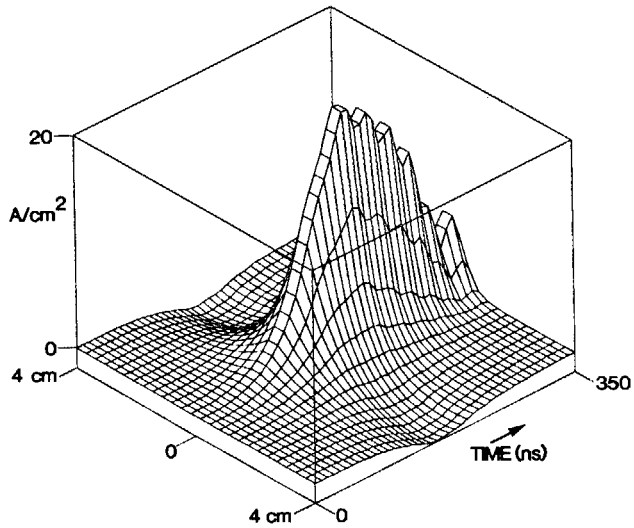

FIG. 15. Increase in current density due to multistep ionization. The conditions are those for the case of nonuniform preionization electron density in Fig. 14. This figure was obtained by recomputing the example in Fig. 14 while excluding multistep processes and subtracting the respective current densities.

D. Multistep ionization of excited states of Hg as a constriction mechanism

In Sec. II D, the mechanisms by which atomic mercury is produced in the HgBr laser were discussed. The existence of mercury in significant quantities in HgBr laser discharges has been confirmed spectroscopically.[11] Using hook method interferometry, a density of excited Hg atoms ($6^3P_{0,1,2}$) of $10^{15}/cm^3$ has been measured for typical discharge conditions. The importance of excited mercury in the discharge is clear from the plots of electron impact excitation rates in Fig. 4. The largest rates are for ionization of excited states of mercury. The accumulation of mercury in the discharge promotes the tendency towards constriction due to the ease with which its excited states are ionized.[9] Multistep processes involving excited states of other species, such as $HgBr_2^*$,[6] also contribute to rapid ionization and subsequent constriction. For our conditions, though, we found multistep processes involving mercury atoms to be the dominant contributor.

The sequences of events by which multistep ionization of mercury can lead to constriction of the discharge is illustrated in Fig. 16, where the fraction of ions belonging to $HgBr_2^+$, $HgBr^+$, and Hg^+ are plotted for typical laser discharge conditions. Early in the discharge, the dominant ion is $HgBr_2^+$. At these times, the electron density is low and, as a result, the densities of HgBr or excited states of $HgBr_2$ are also low. The majority of $HgBr_2^+$ therefore results from the single-step ionization of ground-state $HgBr_2$. As the discharge proceeds and the electron density increases, HgBr begins to accumulate as a result of dissociative electron collisions with $HgBr_2$, and the reservoir of $HgBr_2$ begins to become depleted. A large density of excited states of HgBr also

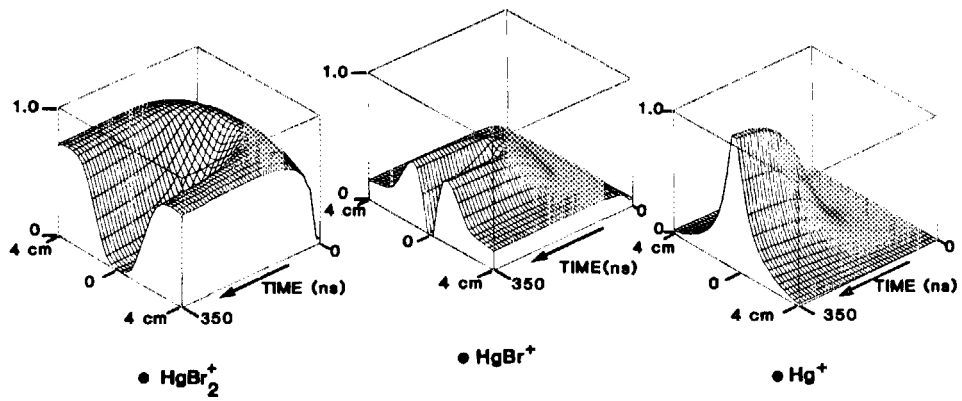

FIG. 16. Calculated fraction of ions belonging to $HgBr_2^+$, $HgBr^+$, and Hg^+. The dominant ion in the constricted core is Hg^+, however, the dominant ion remains $HgBr_2^+$ in regions where multistep electron impact processes are not important. Note the reversal of the time axis.

begins to accumulate. As a result of their lower ionization potential and subsequently larger rates of ionization, the role of the dominant ion is now shared between $HgBr_2^+$ and $HgBr^+$. Note that in the outer regions of the discharge where the electron density is low and multistep excitation processes are not important, the dominant ion remains $HgBr_2^+$, a result of single-step ionization. As the discharge progresses, the constricted core becomes clearly delineated by the region in which Hg^+ becomes the dominant ion. This dominance results in large part from multistep ionization of excited states of Hg and less so from depletion of $HgBr_2$. In this core, the density of $HgBr_2$ is $6.7\times10^{16}/cm^3$, depleted to only 0.45 that of its initial value. The rate constant for ground state ionization of $HgBr_2$, though, is 8×10^{-12} cm^3/s, yielding an ionization rate of $5.4\times10^5/s$. The density of mercury atoms in excited states is more than an order of magnitude less than that of the $HgBr_2$; however, a rate constant for ionization of 4×10^{-8} cm^3/s yields an ionization rate for excited mercury of $1.6\times10^8/s$, a factor of 300 times larger than that of ground-state $HgBr_2$.

A secondary but significant effect with respect to multistep ionization processes is that as the impedance of the discharge decreases, the voltage drop across the electrodes and, hence, the value of E/N, also decreases. In the E/N range of interest (about 4×10^{-17} V cm^2), the average electron energy is about 3 eV, and the rate of decrease in the ionization rate constant for $HgBr_2$ is larger than that of the excited states of Hg. (See Fig. 4.) [Recall that the ionization potential of $HgBr_2$ (10.6 eV) is much larger than that of the excited states of Hg (4.8 and 5.6 eV) and, hence, is more sensitive to changes in applied electric field when the average electron energy is significantly below threshold.] Therefore, not only is the rate of ionization for $HgBr_2$ smaller than that of Hg*, it is also decreasing at a faster rate as the applied E/N decreases. This nonlinear behavior explains why voltage transients can be detrimental to laser performance and discharge stability, and why *e*-beam and *e*-beam sustained discharges have obtained higher efficiencies than discharge excited lasers.[6] Voltage transients which are more likely to occur in self-sustained avalanche devices can push excitation rates into a regime which emphasizes the relative importance of multistep processes at isolated locations in the discharge. The trend promotes unstable behavior and leads to constriction.

E. Impedance matching

When viewed as a circuit element, the discharge is a time varying, voltage- and current-dependent resistance. When combined with the geometrical inductance and capacitance of the laser head, the discharge provides a dynamic terminating load impedance to the electrical PFL. Maximum energy is transferred from the PFL to the terminating load during the first round-trip transit time of the voltage pulse when the impedance of the terminating resistor is equal to that of the PFL. For well-matched conditions, the energy transfer can be near unity. For mismatched conditions, the energy transfer will be much less then unity.

As the stored electrical energy in the PFL increases and the amount of energy deposited in the discharge increases, the electron density increases and the $HgBr_2$ density decreases. Therefore, when viewed as a circuit element, and for otherwised fixed conditions, the impedance of the discharge decreases with increasing stored energy. The implication of this statement is that the optimum impedance (with respect to laser efficiency) of the PFL for an HgBr laser should decrease with increasing stored electrical energy. Equivalently, laser efficiency should optimize at higher stored energy as the impedance of the PFL decreases. This is merely a restatement that maximum energy is transferred to the load of a PFL when the impedances are matched, an effect that is especially important for HgBr lasers. For lasers in which the discharge and PFL have not been optimally matched, this effect in large part explains the behavior observed when additives such as N_2 are used in the gas mix. By use of such additives, impedance matching of the discharge to the PFL can be improved. Therefore, laser efficiency increases as a result of more energy being deposited in the discharge rather than as a result of a change in the excitation mechanism.

To illustrate the interdependence of laser efficiency, stored electrical energy, and PFL impedance, a set of calculations was performed parameterizing these variables. In order to isolate the impedance matching effect, the discharge was not allowed to constrict and the initial $HgBr_2$ density was chosen sufficiently large that depletion was not an important consideration. Computationally, the former effect was accomplished by having only a single vertical discharge region in the model whose width is equal to the desired discharge width. The results of this parameterization are plotted in Fig. 17 where the optimum PFN line impedance is plotted as a function of stored electrical energy. Laser efficiency optimizes at lower PFN impedance for higher stored energy. This optimization is due in large part to better impedance matching of the discharge to the PFN as the discharge becomes more conductive, thereby allowing a higher energy transfer efficiency from the PFN to the laser discharge.

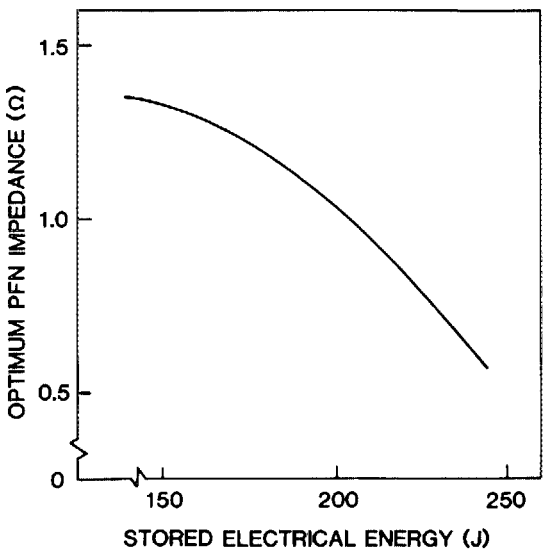

FIG. 17. Calculated optimum PFN impedance as a function of stored electrical energy.

V. PARASITIC DISCHARGE FORMATION AND DEPENDANCE OF LASER ENERGY ON PREIONIZATION ELECTRON DENSITY

A. Parasitic discharges

Parasitic discharges are discharge paths between the electrodes which are outside the limits of the optical cavity. These parasitic discharges are either streamers or corona and can be thought of as being a resistance parallel to that of the desired laser discharge. Parasitic discharges represent both an energy loss mechanism and a mechanism by which the E/N and, hence, the excitation rates for the main discharge are decreased. The latter effect is a result of the pair of discharges (desired and parasitic) creating a lower combined parallel resistance than the main discharge alone. The formation of parasitic discharges has recently been identified as a major limiting effect when attempting to scale excimer lasers to large volumes.[44] In order to prevent the formation of these parasitics, arc tracking retarders are often built into the side walls of the discharge. These retarders increase the effective path length for the parasitics, thereby decreasing the E/N for their excitation.

The shortest anode-cathode path and, hence, the largest average E/N is between the discharge electrodes. Therefore, if the gas is preionized predominantly between the electrodes, the discharge should remain constrained to that region. In order for a discharge to develop in a region other than between the electrodes, there must be a geometrical or materials effect which increases the local electric field or increases the local rate of ionization in that region. An example of the former effect is sharp edges on an electrode feedthrough structure which enhances the local electric field, thereby enabling a streamer or corona discharge to develop. An example of the latter effect is material sputtering from a wall that introduces into the discharge an atom or molecule with a significantly lower ionization potential than the ambient gas.

Television camera photography of our HgBr discharge revealed that significant fluorescence was coming from the rear of the electrode structure in our laboratory laser. This fluorescence, which was also observed in the absence of preionization, correlated with the laser operating at less than optimum efficiency and a discharge voltage which dropped more rapidly than in the absence of this fluorescence. These observations led us to the conclusion that a parasitic discharge was developing from the back side of the electrode structure which competed with the main discharge in the manner described above. The origin of the parasitic discharge was tentatively identified as electric field enhancement at sharp edges in the electrode structure. This identification was confirmed by rounding and shielding those edges and observing a reduction in parasitic fluorescence.

The degree to which parasitic discharges of this type are able to decrease laser efficiency was investigated with the model. The parasitic discharge was treated in the same manner as the main discharge. That is, the same electron and heavy particle collision processes were calculated for the parasitic discharge as for the main discharge. Laser intensity, though, was not calculated for the parasitic region since it is outside of the optical cavity. The discharge path (the effective distance between the electrodes) for the parasitic discharge was estimated to be 12 cm, about twice that of the main discharge. The width of the parasitic discharge was estimated to be 2 cm, about 1/3 that of the main discharge. The preionization electron density for the parasitic discharge was half that of the main discharge. The electric field enhancement was treated in the following manner.

From oscilloscope traces of voltage on the laser head in the absence of preionization between the electrodes, it was estimated that the time required for the parasitic discharge to form and propagate between anode and cathode is 20 ns. We specified a degree of electric field enhancement for the parasitic discharge and linearly decreased the enhancement from its initial value to unity during the 20 ns required for closure. We considered this an optimistic case since some local electric field enhancement around the sharp edges will still take place after closure. The local electric field enhancement in the region directly adjacent to the sharp edges for our laboratory laser was calculated to be about 15.[45] The electric field enhancement factor used in the model is an effective average over the path length and therefore is somewhat smaller than this maximum value. Average electric field enhancement factors of 6–7 were found to be sufficient to reduce laser efficiency by half. The fraction of current which flows through the parasitic discharges for these values of enhancement is roughly 20%. The sensitivity of laser efficiency to parasitic discharges was found to be a function of the preionization electron density. This effect is discussed below.

B. Dependence of laser pulse energy on preionization electron density

It has been experimentally observed that laser pulse energy decreases as the preionization electron density (PED) is decreased. Over a range of PED of 10^9–10^7 cm^{-3}, laser pulse energy decreases by a factor of 2.[11] Laser pulse energy is critically dependent on the PED if this value is below that required to initiate a homogeneous discharge. The requirement on PED for a homogeneous discharge is that the average distance between preionization electrons be less than the radius of the avalanche streamer initiated by that electron[46];

$$\left(\frac{1}{n_{e0}}\right)^{1/3} < r_s \approx \left(\frac{2C_e}{3u_e}\xi_c\lambda_e\right)^{1/2}, \tag{21}$$

where r_s is the radius of the streamer, u_e is the electron drift velocity, C_e is the electron thermal speed, ξ_c is the avalanche track length, and λ_e is the electron mean free path. For discharge conditions typical for HgBr lasers, Eq. (21) is satisfied if $n_{e0} > 5\times 10^5$, a value that was always exceeded in our experiments.

The effect of PED on laser pulse energy was also examined with our model. In the absence of geometrical effects, the results were almost insensitive to changes in the PED for the range of values discussed above. Laser pulse energy decreased by only about 5%. The time required for avalanche of the discharge measured from triggering of the spark gaps, though, did increase as the PED decreased, and details of the voltage waveforms changed. The net result with respect to laser pulse energy was expected as there are no processes

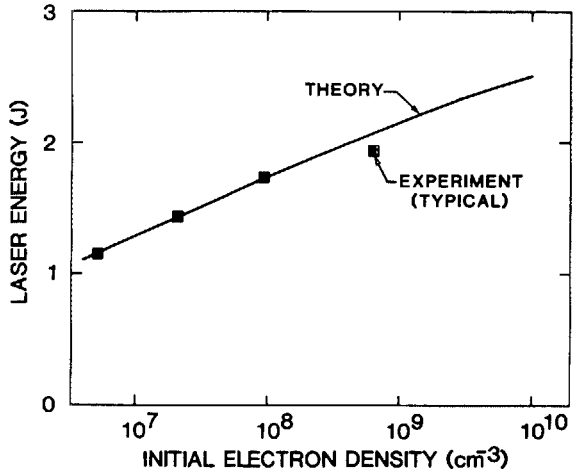

FIG. 18. Laser efficiency as a function of preionization electron density. The squares are experimental data. The line represents results from the model using a field enhancement factor of eight for the parasitic discharge. The field enhancement applies for at most the first 20 ns of formation of the parasitic discharge.

included in the reaction scheme that are critically dependent on the initial electron density. When parasitic discharges were included in the calculation in the manner described in Sec. V A, a sensitive dependance of laser pulse energy on the PED resulted (see Fig. 18). Using the average electric field enhancement factor for the parasitic discharge as a parameter, excellent agreement with experiment was obtained with an enhancement of about 8. For our experimental conditions, parasitic discharge formation appears to have been a factor in reducing laser pulse energy at low PED.

VI. CONCLUDING REMARKS

A multidimensional model for transverse avalanche electric discharges has been described. The model has been applied to study geometrical effects within the discharge region of a HgBr laser. Constriction of the discharge has been examined as a function of electrode contours, preionization electron density profile, and of the rate of power deposition. For conditions where the $HgBr_2$ density is not depleted, constriction of the discharge does not significantly reduce the total laser pulse energy. The uniformity of the laser output intensity and, hence, its propagation potential does suffer. Constriction of the discharge and subsequent impedance collapse is in large part responsible for the observed decrease in laser efficiency as the stored electrical energy increases. Some portion of this decrease is a result of impedance mismatch between the discharge region and the PFL. Multistep ionization from excited states of $HgBr_2$, HgBr, and, in particular, Hg contribute to the rapid constriction of the discharge. The dominant ion in the constricted core of the discharge is Hg^+. Only mild amounts of electric field enhancement are required outside of the main discharge region in order to create a parasitic discharge of sufficient magnitude to significantly reduce laser efficiency. Parasitic discharges may, in part, be responsible for the observed decrease in laser pulse energy as the preionization electron density decreases. Eliminating points of electric field enhancement outside the desired discharge region and maintaining preionization electron density profiles and electrode contours (i.e., E/N) to a maximum variation of 10% should insure a stable discharge in HgBr lasers and serve to maximize laser efficiency. Following these steps, laser energy from our 1-m-long electric discharge HgBr laser could increase approximately 50% from the presently demonstrated 1.3 J/l to almost 2.0 J/l. An efficiency of 3%, similar to the value obtained in *e*-beam sustained discharges, appears possible.

ACKNOWLEDGMENT

This work was performed with Spectra Technology/ Mathematical Sciences Northwest Independent Research and Development support.

[1]E. J. Schimitschek and J. E. Celto, Opt. Lett. **2**, 64 (1978).
[2]R. Burnham, Appl. Phys. Lett. **33**, 156 (1978).
[3]E. J. Schimitschek and J. E. Celto, Appl. Phys. Lett. **36**, 176 (1980).
[4]W. T. Whitney, Appl. Phys. Lett. **32**, 239 (1978).
[5]R. T. Brown and W. L. Nighan, Appl. Phys. Lett. **37**, 1057 (1980).
[6]J. C. Hsia, M. W. McGeoch, and D. E. Klimek, "Space-Based Blue-Green Laser," AVCO Final Report, Contract No. N00123-80-C-1135, October 1981.
[7]J. H. Parks, Appl. Phys. Lett. **31**, 297 (1977).
[8]E. J. Schimitschek, J. E. Celto, and J. A. Trias, Appl. Phys. Lett. **31**, 608 (1977).
[9]C. H. Fisher, I. Smilanski, T. A. Znotins, P. E. Cassady, T. R. Burkes, and J. J. Ewing, Conference on Lasers and Electro-Optics, Paper FG2, Phoenix, 1982.
[10]C. H. Fisher, T. A. Znotins, I. Smilanski, A. L. Pindroh, T. E. DeHart, and J. J. Ewing, Conference on Lasers and Electro-optics, Paper FJ2, Baltimore, 1983.
[11]"Final Report: 200 Watt Mercury Bromide Laser," Mathematical Sciences Northwest, Bellevue, WA, Contract No. N66001-81-C-0939, June 1984.
[12]W. L. Nighan, Appl. Phys. Lett. **36**, 173 (1979).
[13]W. L. Nighan and R. T. Brown, J. Appl. Phys. **53**, 7201 (1982).
[14]W. L. Nighan, J. J. Hinchen, and W. J. Wiegand, J. Chem. Phys. **77**, 3442 (1982).
[15]M. W. McGeoch, J. C. Hsia, and D. E. Klimek, J. Chem. Phys. **78**, 1180 (1983).
[16]J. Allison and R. N. Zare, Chem. Phys. **35**, 263 (1978).
[17]R. S. R. Chang and R. Burnham, Appl. Phys. Lett. **36**, 397 (1980).
[18]D. Spence, R.-G. Wang, and M. A. Dillon, Appl. Phys. Lett. **41**, 1021 (1982).
[19]L. E. Kline, C. L. Chen, P. J. Chantry, and L. J. Denes, "Electron Kinetics Analysis for HgBr Lasers Using a Measured B State Excitation Cross Section," Paper FB-3, 35th Gaseous Electronics Conference, Dallas, Texas, 1982.
[20]C. L. Chen and P. J. Chantry, "HgBr* (B) Production by Electron Impact on $HgBr_2$," Paper EB-2, 35th Gaseous Electronics Conference, Dallas, Texas, 1982.
[21]A. N. Malinin, A. K. Shuaikov, and V. S. Shevera, Sov. J. Quantum Electron. **13**, 977 (1983).
[22]L. J. Kieffer, "A Compilation of Electron Collision Cross Section Data for Modeling Gas Discharge Lasers," Joint Institute Laboratory Astrophysics, COM-74-11661, September 1973.
[23]W. L. Morgan, Joint Institute Laboratory Astrophysics Information Center Report No. 19, University of Colorado, 1979.
[24]M. W. McGeoch, J. C. Hsia, and D. E. Klimek, J. Appl. Phys. **54**, 3823 (1983).
[25]A. C. Erlandson and T. A. Cool, Chem. Phys. Lett. **96**, 685 (1983).
[26]C. H. Brau, "Rate Gas Excimers," *Excimer Lasers*, edited by Ch. K. Rhodes (Springer, Berlin, 1979), p. 105.
[27]L. A. Levine, S. E. Moody, E. L. Klosterman, R. E. Center, and J. J. Ewing, J. Quantum Electron **QE-17**, 2282 (1981).
[28]A. Vitols and H. Oskam, Phys. Rev. A **5**, 2618 (1972).

[29]J. G. Eden and R. W. Waynant, Appl. Phys. Lett. **34**, 324 (1979).
[30]W. R. Wadt, J. Chem. Phys. **72**, 2469 (1980).
[31]H. Helvajian, M. Mangir, and C. Wittig, Chem. Phys. Lett. **71**, 177 (1980).
[32]J. K. K. Ip and G. Burns, J. Chem. Phys. **51**, 3414 (1969).
[33]G. Greig, H. E. Gunning, and O. P. Strauz, J. Chem. Phys. **52**, 3684 (1970).
[34]M. Biondi, "Recombination," in *Principles of Laser Plasmas*, edited by G. Bekefi (Wiley-Interscience, New York, 1976), pp. 127–146.
[35]S. D. Rockwood, Phys. Rev. A **8**, 2348 (1973).
[36]K. Kentry, J. Appl. Phys. **21**, 1309 (1950).
[37]L. Vriens, Phys. Lett. **8**, 260 (1964).
[38]S. M. Skippon, M. D. Rabbert, and T. A. King, J. Phys. D **16**, 2435 (1983).
[39]W. W. Rigrod, J. Appl. Phys. **36**, 2487 (1965).
[40]Y. Reuven and M. Baer, J. Quantum Electron. **QE-16**, 1117 (1980).
[41]M. Mitchner and C. H. Kruger, Jr., *Partially Ionized Gases* (Wiley-Interscience, New York, 1973), pp. 146–155.
[42]E. A. Stappaerts, Appl. Phys. Lett. **40**, 1018 (1982).
[43]L. J. Denes, L. E. Kline, and R. R. Mitchell, "Arc Suppression in Excimer Laser Discharges," Proceedings of the SOQE International Conference on Lasers, New Orleans, Louisiana, 1981.
[44]L. F. Champagne, A. J. Dudas and B. L. Wexler, Conference on Lasers and Electro-optics, Paper ThR8-1, Anaheim, 1984.
[45]W. L. Willis, "Spark Gaps," Los Alamos National Laboratory, Rept. No. LA-UR 80-634, 1980.
[46]J. I. Levatter and S. C. Lin, J. Appl. Phys. **51**, 210 (1980).
[47]C. Deutsh, J. Appl. Phys. **44**, 1142 (1973).